

# A Statistical Spatio-Temporal Radio Channel Model for Large Indoor Environments at 60 and 70 GHz

Katsuyuki Haneda, *Member, IEEE*, Jan Järveläinen, Aki Karttunen, *Member, IEEE*, Mikko Kyrö, and Jyri Putkonen

**Abstract**—Millimeter-wave radios operating at unlicensed 60 GHz and licensed 70 GHz bands are attractive solutions to realize short-range backhaul links for flexible wireless network deployment. We present a measurement-based spatio-temporal statistical channel model for short-range millimeter-wave links in large office rooms, shopping mall, and station scenarios. Channel sounding in these scenarios at 60 and 70 GHz revealed that spatio-temporal channel characteristics of the two frequencies are similar, making it possible to use an identical channel model framework to cover the radio frequencies and scenarios. The sounding also revealed dominance of a line-of-sight and specular propagation paths over diffuse scattering because of weak reverberation of propagating energy in the scenarios. The main difference between 60 and 70 GHz channels lies in power levels of the specular propagation paths and diffuse scattering which affect their visibility over the noise level in the measurements, and the speed of power decay as the propagation delay increases. Having defined the channel model framework, a set of model parameters has been derived for each scenario at the two radio frequencies. After specifying the implementation recipe of the proposed channel model, channel model outputs are compared with the measurements to show validity of the channel model framework and implementation. Validity was demonstrated through objective parameters, i.e., pathloss and root-mean-square delay spread, which were not used as defining parameters of the channel model.

**Index Terms**—Channel model, millimeter-wave, short-range communications.

## I. INTRODUCTION

**D**ESIGN of traditional fixed point-to-point microwave or millimeter-wave radio relay systems is based on the assumption that antenna main beam widths are very narrow, side-lobe levels are low, and the beams are pointing to a fixed direction while aligned. These kinds of fixed radio systems are well studied and standardized [1]. Fixed radio relays are nowadays mainly used to provide backhauling traffic for base stations covering mobile cellular scenarios. Due to increased data rates requirements, cell sizes are shrinking and wireless backhaul links can be shorter. Millimeter-wave radio links are

suitable for such short-range high-data-rate links because of the large available bandwidth. There is also a need to relax the directiveness of antenna beam patterns, motivated by network operation with increased flexibility where transceiver locations are only loosely defined and new installations of transceivers take place continuously. These conceptual evolutions in network deployment and their feasibility study call for thorough understanding of millimeter-wave propagation especially in large indoor and short-range urban outdoor environments.

Though measurement-based study of 60 GHz radio propagation modeling is nowadays widely available in literatures, e.g., [2]–[6] and references therein, channel sounding and modeling in other millimeter-wave frequencies are relatively scarce and are only found in [7]–[12], which mostly cover 30 and 70 GHz ranges in outdoor environments. In this paper, we address spatio-temporal characteristics of 70 GHz indoor short-range propagation, based on extensive radio channel sounding reported in [13], to investigate if there are major differences with 60 GHz radio propagation. The sounding was performed in large office rooms, shopping malls, and on platforms of a railway station, which have not been reported much in the previous studies. The work in [13] shows angular and delay characteristics of 60 and 70 GHz indoor radio channels to discuss their differences in terms of the delay spread. The present paper extends the work to develop a novel statistical channel model framework, which is applicable to all the scenarios covered in the measurements and to the two radio frequencies of interests, and to provide channel model parameters for each case. Our channel model characterizes the measured channels by a set of distributions similar to the IEEE 802.15.3c channel model [2], but has a number of differences for better fit to measured channels; e.g., our model distinguishes the specular and diffuse nature of radio propagation [14] and does not take over the concept of multipath clusters. Our model serves as an alternative to a geometry-based channel model that is adopted in different standardization bodies such as 3GPP [15] and ITU-R [16], for simpler model structure. The developed channel model framework and parametrization is verified by comparing channel model outputs with measurements by means of objective metrics, i.e., pathloss and root-mean-square delay spread, which are not used as defining parameters of the channel model. We provide a full mathematical formulation of the proposed channel model, a list of model parameters, and a model implementation recipe to advocate the novelty and significance of the present paper.

This paper consists of five sections: Section II describes the channel sounding apparatus and measurement sites, Section III

Manuscript received July 19, 2014; revised December 15, 2014; accepted September 17, 2015. Date of publication March 11, 2015; date of current version May 29, 2015.

K. Haneda, J. Järveläinen, and A. Karttunen are with Aalto University School of Electrical Engineering, Espoo FI-00076, Finland.

M. Kyrö was with Aalto University School of Electrical Engineering. He is now with the Finnish Patent and Registration Office, Helsinki, Finland.

J. Putkonen is with Nokia Networks, Espoo, Finland (e-mail: jyri.putkonen@nokia.com).

Color versions of one or more of the figures in this paper are available online at <http://ieeexplore.ieee.org>.

Digital Object Identifier 10.1109/TAP.2015.2412147

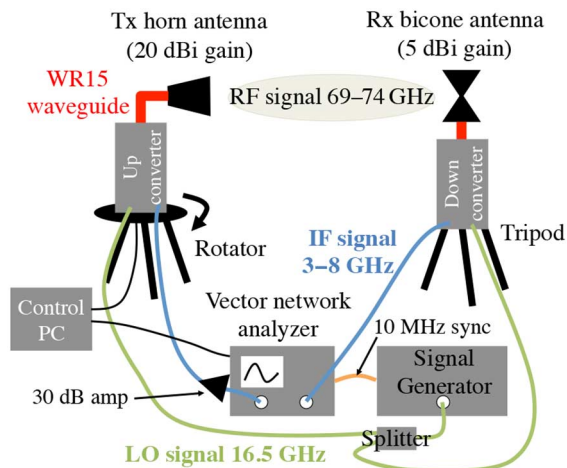


Fig. 1. Schematic of the radio channel sounder at 70 GHz.

provides channel characterization methodologies focusing on the propagation path detection method and definition of diffuse scattering. Section IV presents channel characterization results leading to the proposed channel model framework. Section V details the framework and their parametrization followed by a channel model implementation recipe and their validation. The paper is finally concluded in Section VI.

## II. RADIO CHANNEL SOUNDING

### A. Channel Sounder

Fig. 1 illustrates the radio-frequency (RF) part of the channel sounder. The sounder is based on a vector network analyzer (VNA) that allows us to measure both amplitude and phase of the transfer function of radio channels over large bandwidth. The intermediate frequency (IF) signal at the VNA is swept from 3 to 8 GHz and the frequency up- and down-converters bring it to the RF range from 69 to 74 GHz. A signal generator is used for delivering the 16.5-GHz local oscillator (LO) signal to the frequency converters. The phase of the LO signal is locked to the VNA using a 10-MHz reference signal output from the VNA. By setting the IF range to be from 5 to 9 GHz and the LO frequency to be 14 GHz, RF channel measurements at 61–65 GHz are also realized using the same equipment. The difference of the bandwidth at 60 and 70 GHz stems from the capability of the up- and down-converters. Since channel sounding with wider bandwidth allows finer delay resolution of the channel, we used the maximum available bandwidth of the sounder at each frequency band.

The antennas in the measurements are a standard gain horn and a biconical antenna at the transmit (Tx) and receive (Rx) sides, respectively, which work at the two RF bands. The biconical antenna is omnidirectional on the azimuth plane with 5 dB maximum gain at 60 GHz, while it covers only a narrow range of the elevation angle with  $11^\circ$  half power beamwidth. The horn antenna has about 20 dBi gain [17] with about  $18^\circ$  half power beamwidth both on the azimuth and elevation domains at 60 GHz and with 35 dB cross-polarization discrimination for the main-lobe direction. Going from 60 to 70 GHz, the antennas keep the shape of the main beam of the radiation pattern but with progressive decrease of the gain by about 3 dB.

and narrower beamwidth by  $2^\circ$ . The antennas are fed from/to the up-/down-converters through waveguides and cover the RF range between 60 and 75 GHz. Angular characteristics of propagation channels can be measured by rotating the directional Tx antenna.

### B. Channel Sounding

Indoor channel sounding campaigns have been performed at four sites: 1) an empty office; 2) an office in-use, 3) open spaces in a shopping mall; and 4) a railway station platform. The first three sites are situated in a modern building, while the station is a semi-open space with a transparent roof composed of plastic plates and metal frames. The approximate size of the measurement sites is  $18 \times 22 \times 2.5 \text{ m}^3$  for the offices,  $40 \times 120 \times 20 \text{ m}^3$  for the shopping mall, and  $80 \times 180 \times 8 \text{ m}^3$  for the station scenarios. The office room in-use contains working facilities such as desks, chairs, and low height partitions, while escalators, pillars, and shop tenants surround the antennas in the shopping mall. Building walls, pillars, and parking train wagons are the major reflecting objects in the station platform. Except for the empty office room, there were walking people during the measurements. In this case, the channel transfer function was measured three times successively over time for each rotation angle of the Tx antenna so that the effect of human blockage and the receiver noise is reduced through channel averaging.

The 5- and 4-GHz measurement bandwidths at 70 and 60 GHz frequency bands, respectively, lead to a delay resolution of 0.2 and 0.25 ns. Since the IF sweep at the VNA is performed over 2001 equally spaced frequency points over the measurement bandwidth, the maximum detectable delay is 400 and 500 ns corresponding to 120 and 150 m of the path length. They imply that a scatterer located up to 60 and 75 m away from the antennas can be detected without ambiguity in distance. A direct connection back-to-back calibration is performed before the measurements in order to compensate for the transfer functions of cables, up- and down-converters, and waveguides attached to the antennas. Effects of antenna radiation patterns are therefore a part of radio channels measured in the sounding. During the measurement, the Tx antenna is rotated over  $360^\circ$  azimuth angle, and the channel transfer function was acquired at every azimuth angle. Much denser measurements of channels over the azimuth angles compared to the Tx antenna beamwidth allow precise estimation of the azimuth angular characteristics of radio channels. The Tx and Rx antenna height was 1.94 m above the floor. We restrict the rotation range of the Tx antenna to the  $0^\circ$  elevation angle because of the narrow elevation angle that the Rx antenna illuminates. The Tx–Rx distance was mostly less than 10 m and a line-of-sight between the two antennas was available in most cases. The number of Tx and Rx locations for each measurement site is summarized in Table I.

## III. CHARACTERIZATION OF THE RADIO CHANNELS

### A. Power Angular and Delay Profiles

A power delay profile (PDP) of a radio channel usually results from the ensemble average of channel impulse responses

TABLE I  
NUMBER OF TX AND RX ANTENNA LOCATIONS IN  
MEASUREMENT SITES

Site	No. of Tx locations	No. of Rx locations	Total no. of measurements	Tx-Rx range (m)
Empty office	13	2	15	1.8–10.3
Office in use	9	2	9	1.1–8.0
Shopping mall	24	3	24	1.4–8.6
Station	8	3	9	0.9–5.6

obtained under the wide-sense stationary condition where the pathloss and shadowing remains constant [18]. With slight violation of the original definition, we derive the PDP by the ensemble average of channel impulse responses obtained with the Tx antenna pointing at different azimuth angles that are subject to varying pathloss and shadowing due to the high directivity of the Tx antenna. Such PDP is still valid for the propagation path detection and analyzing the dominant multipath components in radio propagation, which is the goal of this work.

Let us define a channel transfer function matrix with the Tx antenna pointing at the  $i$ th angle,  $1 \leq i \leq I = 360$ , be  $H_{ij}$  where  $j$  denotes an index of RF sweep,  $1 \leq j \leq J = 2001$  in our measurements. The channel impulse response  $h_i(\tau)$  for the  $i$ th pointing angle is derived by

$$h_i(\tau) = \sum_{j=1}^J w_j H_{ij} \exp(j2\pi f_j \tau) \quad (1)$$

where  $\tau$  is the delay time and  $w_j$  is a window function to reduce a sidelobe level. In our data processing, the Hamming window was used. The power angular delay profile (PADP) is given by  $P_i(\tau) = |h_i(\tau)|^2$ . The PDP is finally derived by the marginal integral of the PADP as  $P(\tau) = \frac{1}{I} \sum_i P_i(\tau)$ .

### B. Path Detection

We define a propagation path as a distinguishable peak in the PDP and PADP, which originates from specular propagation mechanisms. The propagation paths are detected in two steps. In order to avoid a complex multidimensional peak search, peaks are first identified in PDPs. The peak identification is performed by finding local maxima of the PDP curve, followed by a comparison of their levels with a corresponding threshold function, which is defined as

$$T(\tau) = \frac{\epsilon}{\Delta} \int_{\tau-\Delta/2}^{\tau+\Delta/2} P(x) dx \quad (2)$$

where  $\Delta$  is a length of a sliding window over the delay and  $\epsilon$  is an offset of the threshold to avoid detecting artifacts and noisy peaks. Peaks are recognized as paths if their levels are greater than the threshold, giving rise to the parameter estimates of  $L$  paths with respect to delay  $\tau_l$  and gain  $\alpha'_l$ ,  $1 \leq l \leq L$ . Then, their azimuth angles at the Tx antenna are estimated by searching a maximum of the PADP at the identified delays. It is assumed that each delay bin contains only a single peak, which

is reasonable because of the fine delay resolution of the channel sounder. The resultant estimated parameters of the propagation paths are their delays, azimuth angles at the Tx antenna  $\phi_l$ , and gain  $\alpha_l$ . The gain estimated in the PADP is always greater than that in the PDP

$$\alpha_l = G_d \alpha'_l, G_d > 1 \quad (3)$$

because of the gain of Tx antenna pointing to the propagation path;  $G_d$  denotes a gain difference that is fairly constant over the paths.

### C. Diffuse Spectrum

When modeling the radio propagation channel by a set of discrete paths due to specular propagation mechanisms, it is necessary to justify the amount of power modeled by them. This is because the radio channels can also be expressed as continuous spectrum due to distributed diffuse scattering [14]. Usually, the radio channels are expressed by a sum of discrete paths and continuous spectrum, and depending on the propagation scenario, the diffuse spectrum can dominate the radio propagation mechanisms even in millimeter-wave radio channels as reported in [19].

The portion of power modeled by propagation paths is given in the PDP as  $P_{\text{spec}} = \sum_{l=1}^L \alpha'_l$ , while the total received power is derived from the PDP by

$$P_{\text{tot}} = \int_{\tau=0}^{\tau_{\text{max}}} \hat{P}(\tau) d\tau \quad (4)$$

where  $\tau_{\text{max}}$  is the maximum detectable delay and  $\hat{P}$  is a noise-reduced PDP defined as

$$\hat{P}(\tau) = \begin{cases} P(\tau), & \text{if } P(\tau) > T(\tau_n) \\ 0, & \text{if } P(\tau) \leq T(\tau_n) \end{cases} \quad (5)$$

where  $T(\tau_n)$  is given in (2) representing a noise level estimate at  $\tau_n$ ; no signals are present at  $\tau_n$  because of too long delays. The power of propagation paths relative to the total power is finally derived by  $P_{\text{spec}}/P_{\text{tot}}$ .

## IV. ANGULAR AND DELAY CHARACTERISTICS OF THE RADIO CHANNELS

In this section, path detection results are illustrated to infer a possible radio channel modeling structure.

### A. PDPs

Fig. 2 shows an exemplary PDP from the office in-use at the two radio frequencies measured exactly at the same Tx and Rx locations. The figures also show the threshold functions for noise and peak detection as well as the detected peaks. The parameters for deriving the threshold functions are summarized in Table II. The figures demonstrate feasibility of the



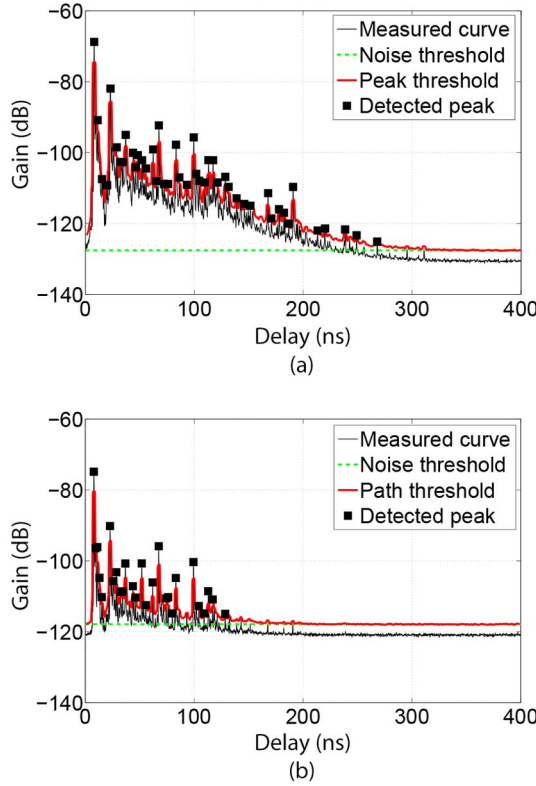


Fig. 2. Exemplary PDPs in the office in-use (a) 60 and (b) 70 GHz. The PDPs were measured at the same Tx and Rx location. Threshold functions for noise and peak detection, and detected peaks are overlaid.

TABLE II  
PARAMETER VALUES IN PROPAGATION PATH CHARACTERIZATION  
AND MODELING

Symbols	Eq.	Values or function
$w_j$	(1)	Hamming window
$\Delta$	(2)	1.25 ns (60 GHz), 1.0 ns (70 GHz)
$\epsilon$	(2)	3 dB
$G_d$	(3)	13.5 dB
$\tau_n$	(5)	350 ns
$L_w$	(7)	4 dB
$G_{ant}$	(7)	23.6 dB (60 GHz), 21.6 dB (70 GHz)

path detection method summarized in Section III. The PDPs are dominated by specular paths represented by spiky peaks at both radio frequencies. Due to a difference in the dynamic range of the channel sounder, antenna gain, and losses in radio propagation, the number of visible specular paths is less at 70 GHz than 60 GHz. However, delays of the major specular paths remain the same at the two frequency bands as expected. In addition to the specular paths, the PDP at 60 GHz shows continuous power spectrum exponentially decaying over the delay, though the power level is much weaker than the specular paths. It is interesting to note that such continuous spectrum was almost negligible in the mentioned example of Fig. 2(b) at 70 GHz. The shape of PDPs governed by the specular peaks is different from typical PDPs observed in confined indoor rooms reported in, e.g., [20], where continuous spectrum decaying exponentially over the delay time is also present on top of the specular peaks. The difference possibly stems from the area size of propagation environments and the density of fixtures in the environment.

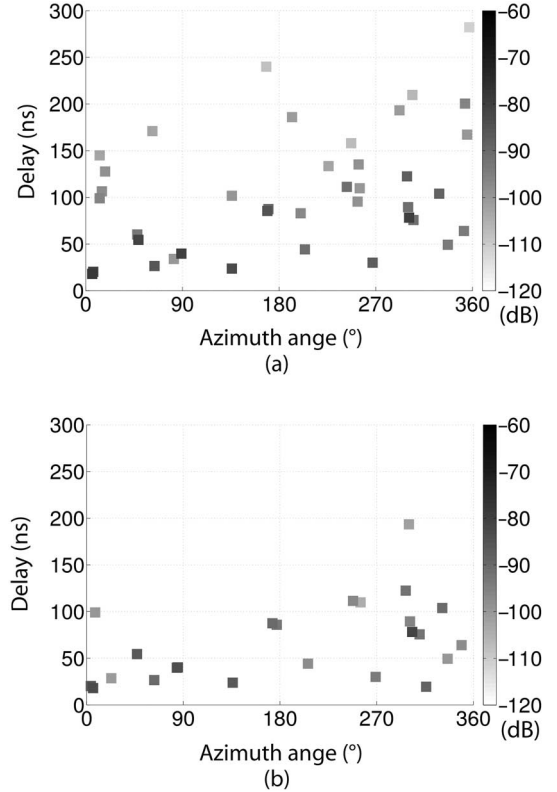


Fig. 3. Path distribution over angular-delay domain in the empty office scenario measured at (a) 60 and (b) 70 GHz. The color bar denotes the path gain estimate  $\alpha_l$ . They were obtained from the same Tx–Rx locations.

Larger area size and lower density of fixtures leads to less reverberation and cluttering of electromagnetic fields inside, which is the cause of the continuous delay spectrum [21].

### B. Path Distribution on the Angular-Delay Domain

Fig. 3 shows exemplary distributions of the detected propagation paths over the angular-delay domain for the empty office scenario. Two important insights are heuristically obtained from the plots: 1) path clustering behavior is not apparent in the angular-delay domain; and 2) the paths are uniformly distributed over  $[0^\circ 360^\circ)$ . Concerning the first insight, the plots *do* show a clustering behavior of paths where a strong path is accompanied by several weaker paths at close-by angles and delays, e.g., the paths with  $300^\circ$  azimuth and 70 ns delay, but most paths exist without an accompanying path. The insight was applicable to all the power angular-delay path distributions obtained from the measurements. The insights lead to a possibility of a simple radio channel model structure without clusters unlike available channel models at the millimeter-wave radio frequencies, e.g., IEEE 802.15.3c and 802.11ad channel models [2], [3], which both consider clusters as an inherent structure of the angular and delay domain path behaviors.

### C. Diffuse Spectrum

Fig. 4(a) illustrates an exemplary diffuse spectrum in the empty office scenario at 60 GHz. The spectrum has a sharp

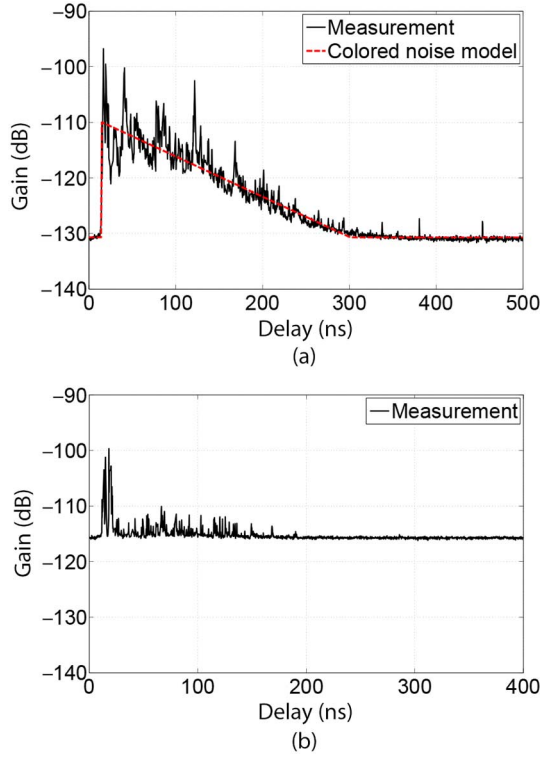


Fig. 4. Exemplary PDP after subtraction of propagation paths and their fit to the model (6). The examples are from (a) empty office at 60 GHz and (b) shopping mall at 70 GHz.

onset at a delay close to the line-of-sight path, which is extracted as a specular path already and hence is not visible on the graph, followed by exponentially decaying power spectrum until it hits the noise level. This type of spectrum has been reported in many channel modeling campaigns at lower frequencies, e.g., [14], as well as at 60 GHz [19] and is commonly modeled as

$$P_{\text{dif}}(\tau) = \begin{cases} P_n & (\tau < \tau_0) \\ P_d/2 & (\tau = \tau_0) \\ \max \{P_n, P_d \exp(-\tau/\beta_d)\} & (\tau > \tau_0) \end{cases} \quad (6)$$

The best fit of the model to the diffuse spectrum is overlaid for 60 GHz empty office scenario in Fig. 4(a) with model parameter summarized in Table III. The model parameters giving the best fit to the measurements were obtained by a numerical search of the parameters with minimum mean square error criterion on the dB-domain. The diffuse spectrum can be described by the model (6) well in 60 GHz measurements in offices and a shopping mall and 70 GHz measurements in office scenarios. The exception is the shopping mall scenario at 70 GHz and the station scenario, where the diffuse spectrum was not seen in the graph because of the low level of the diffuse spectrum and a higher measurement noise floor level at 70 GHz as illustrated in Fig. 4(b).

Fig. 5 shows the ratio of power carried by the line-of-sight (LOS) and specular paths relative to the total power,  $P_{\text{spec}}/P_{\text{tot}}$ , plotted over Tx–Rx distance in the office in-use,

shopping mall and station scenarios. The figures reveal dominance of the LOS and specular propagation mechanism which occupies more than 75% of the total power. The dominance in a short-range line-of-sight open hall environment is consistent with that reported at 5.3 GHz [22]. The dominance is most apparent in spacious and open environments such as the shopping mall and station scenarios where it was always more than 90%, while it was lower in the enclosed office environments. The results lead to an observation that the dominance of the LOS and specular paths is more pronounced as its area size is larger, which is also related to the reverberation of electromagnetic waves. In general, the dominance decreases as the Tx–Rx distance increases. However, if the Tx and Rx antennas are surrounded by fixtures that lead to path shadowing and cluttering, the dominance can be low even with short Tx–Rx distances as demonstrated in the office in-use scenario in Fig. 5(a) for the distance less than 3 m. The closer the fixtures are to the antennas, the less dominant the specular paths tend to be since the closer fixtures are well illuminated by the antennas and create diffuse scattering from their surface profiles.

## V. PROPAGATION CHANNEL MODEL

This section introduces a novel propagation channel model for large indoor open halls, which is proposed based on the channel characterization results described in the previous sections. Angular-delay domain representations of the specular and diffuse paths are presented followed by their parametrization using our measurements.

### A. Path Gain Correction

It is necessary to apply two types of gain correction for the paths from measurements in order to develop a meaningful propagation channel model. They are 1) corrections of antenna gain; and 2) power loss due to the window function. In performing the Fourier transform in (1), a window function is applied to reduce sidelobe levels while it also reduces the peak levels. For the Hamming window we used in (1), approximately  $L_w = 4$  dB is lost compared to the rectangular window and this is the power that has to be compensated for the paths.<sup>1</sup> The power loss due to the window and the gain of the Tx and Rx antennas are compensated from the estimated gain of the propagation path by

$$\hat{\alpha} = \alpha L_w / G_{\text{ant}} \quad (7)$$

where  $\hat{\alpha}$  represents the gain during the radio propagation and  $G_{\text{ant}}$  denotes the combined Tx and Rx antenna main-lobe gains considering the fact that the paths were detected while illuminated by antenna main-lobes. An assumption here is that the radio propagation occurs mainly on the horizontal plane because of the identical height of Tx and Rx antennas and also because of the narrow half-gain beamwidth of the Tx and Rx antennas, i.e.,  $11^\circ$  and  $20^\circ$  for the elevation direction, respectively.

<sup>1</sup>The power loss due to the Hamming window was calculated by  $L_w = 10 \log_{10}(\frac{1}{J} \sum_{j=1}^J |w_j|^2)$ , where  $w_j$  is a weighting coefficient of the Hamming window,  $1 \leq j \leq J = 2001$ .

TABLE III  
CHANNEL MODEL PARAMETERS

Symbols	Units	Eq.	Empty office		Office in-use		Shopping mall		Station	
			60 GHz	70 GHz	60 GHz	70 GHz	60 GHz	70 GHz	60 GHz	70 GHz
$P_d$	dB	(6)	-105.6	-111.5	-103.9	-109.6	-113.4	N/A	N/A	N/A
$\beta_d$	ns	(6)	144.1	333.7	129.0	257.1	209.9	N/A	N/A	N/A
$P_0$	dB	(8)	-107.7	-107.2	-105.7	-106.1	-110.2	-106.6	-112.2	-107.9
$\beta_0$	ns	(8)	112.0	98.0	100.0	84.0	106.0	90.0	110.0	78.1
$\tau_c$	ns	(8)	304	217	244	185	197	133	450	200
$\sigma_s$	dB	(9)	8.1	7.6	8.0	7.8	7.3	7.5	8.7	8.9
$\beta_{p0}$	ns	(15)	1.6	0.2	3.1	2.3	0.8	3.9	0.0	2.6
$\beta_s$		(15)	5.4	10.2	2.9	5.6	5.6	6.0	5.9	10.8

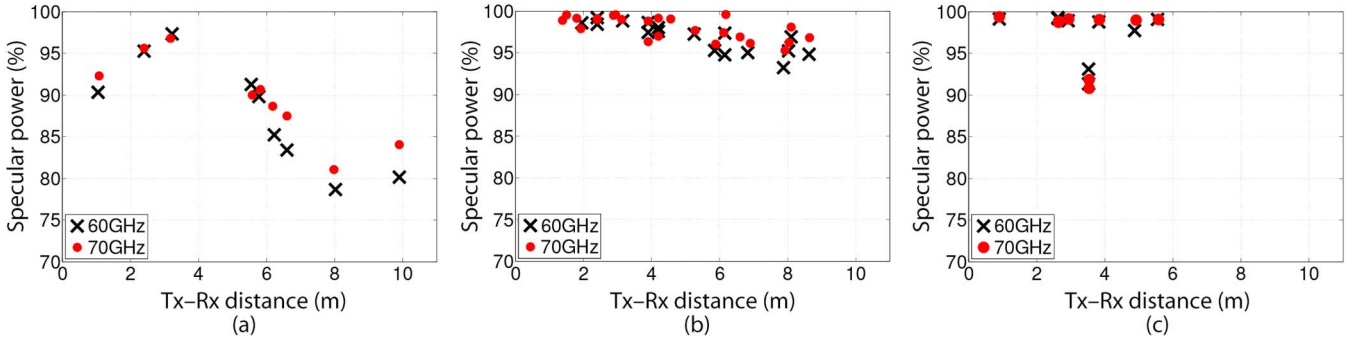


Fig. 5. Ratio of specular power relative to the total power in (a) office in-use; (b) shopping mall; and (c) station.

### B. Power Decay and Shadow Fading Model

The underlying model of the power decay characteristics of propagation paths excluding the line-of-sight paths is given by

$$\hat{\alpha}_l = P_0 \exp(-\tau_l/\beta_0)\xi, \quad 0 < \tau < \tau_c \quad (8)$$

where  $P_0$  is initial pathloss,  $\beta_0$  is a power decay factor, and  $\xi$  is a normal random variable in the dB scale as

$$10 \log_{10} \xi \sim \mathcal{N}(0, \sigma_s^2) \quad (9)$$

where  $\sigma_s$  is the standard deviation of the shadow fading, and finally  $\tau_c$  is a maximum delay for which the model is valid. In order to estimate the parameters of the model, a likelihood function is formulated as

$$LF = \prod_{l=1}^L \frac{1}{p_l \sigma_s \sqrt{2\pi}} \exp \left\{ -\frac{(P_l - P_m)^2}{2\sigma_s^2} \right\} \quad (10)$$

where  $P_l = 10 \log_{10} \hat{\alpha}_l$ ,  $P_m = 10 \log_{10} \{P_0 \exp(-\tau_l/\beta_0)\}$ . The likelihood function considers a probability  $p_l$  that the power of the  $l$ th specular path is above the noise level [23]. In our case, the noise is colored as represented by the diffuse spectrum  $P_{dif}$  in (6). It is necessary to consider the probability since the parameters of the power decay constant has to be estimated using a portion of propagation paths visible over the colored noise level. The idea is to recognize hidden propagation paths below the noise level that could not be detected in the measurements. The probability is defined by the complementary error function  $\text{erfc}(\cdot)$  as

$$p_l = \frac{1}{2} \text{erfc} \left( \frac{\hat{P}_{dif}(\tau) - P_l}{\sqrt{2}\sigma_s} \right) \quad (11)$$

where  $\hat{P}_{dif}(\tau) = G_d P_{dif}(\tau) L_w / G_{ant}$  is a colored noise model in the angular-delay domain with antenna gain subtraction. A log-likelihood function yields from (10) as

$$LLF = \sum_{l=1}^L \left\{ \ln(p_l \sigma_s) + \frac{(P_l - P_m)^2}{2\sigma_s^2} \right\} \quad (12)$$

which is used to find the model parameters of interests by

$$(P_0^*, \beta_0^*, \sigma_s^*) = \arg \min_{P_0, \beta_0, \sigma_s} LLF \quad (13)$$

where  $\cdot^*$  denotes a maximum likelihood estimate. The model parameters were derived for each measurement scenario. Within a measurement scenario, the same model parameters seem to be valid according to the plots in Fig. 6 which include all the paths detected in the measurement scenario. The mean power decay curves  $P_m$  estimated from the paths are overlaid in the plots. It should be noted that the model is invalid beyond a delay  $\tau_c$ , where the power decay slope seems to change from that at the smaller delay, but the number of paths are too small to obtain a valid model.

### C. Other Features of the Model

1) *Angular Path Distribution*: According to the observations in Section IV-B, the angular distribution of the paths can be approximated by the uniform distribution in all the measurement scenarios. Fig. 7 verifies the observation which shows the cdfs of azimuth angles at the Tx side for the empty office and shopping mall scenarios at 60 and 70 GHz. The number of measured channels with different Tx and Rx locations is an influential parameter determining the proximity of the measured curve with the uniform distribution. The office

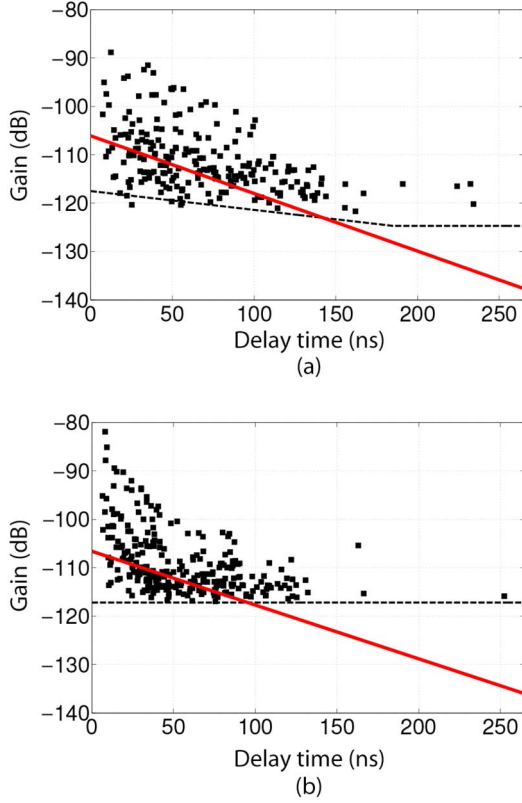


Fig. 6. Propagation path profile on the delay domain. All detected paths from (a) office in-use; and (b) shopping mall scenarios at 70 GHz are plotted in the figures. The red and black dashed lines represent estimated mean decay and the colored noise, respectively.

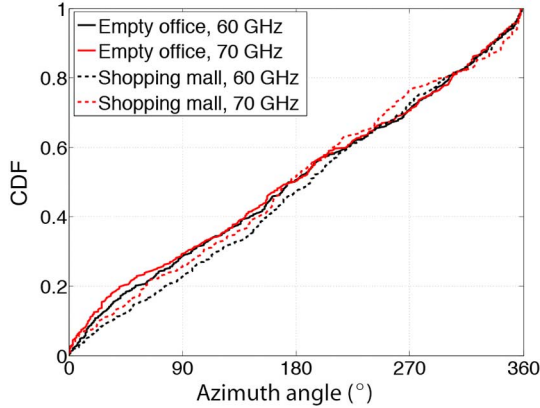


Fig. 7. Path arrival angle cdf in empty office and shopping mall scenarios. Results with 60 and 70 GHz measurements are shown.

in-use scenario where the number of measurement samples is the smallest showed slight deviation of the arrival angle distributions from the uniform distribution.

2) *Path Arrival Rate*: As reported in many available channel models, it is reasonable to approximate the path arrival rate using the Poisson process with the interpath delay following the exponential distribution. The distribution is given by

$$p_{\text{path}}(\tau_{l+1}|\tau_l) = \exp\left(-\frac{1}{\beta_p} \cdot \frac{\tau_{l+1} - \tau_l}{1 - p_l}\right) \quad (14)$$

$$\beta_p = \beta_{p0} + \frac{\beta_s}{100} \tau_l \quad (15)$$

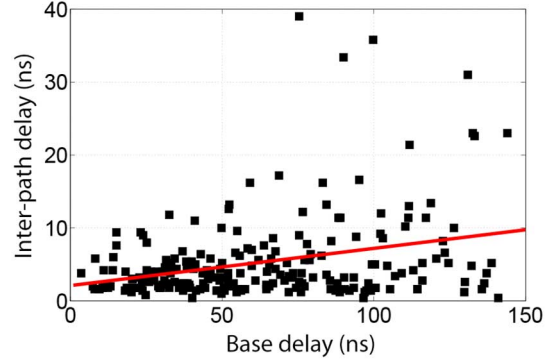


Fig. 8. Interpath delay with respect to the base delay measured in the office in-use scenario at 70 GHz.

where  $\beta_p$  denotes the mean interpath delay which was found dependent on the base delay  $\tau_l$  as shown in (15). Less paths tend to arrive at larger delays and  $\tau_l$  is in nanoseconds. The term  $(1 - p_l)$  in the denominator of (14) compensates for the existence of hidden paths below the noise level. The parameters  $\beta_{p0}$  and  $\beta_s$  in (15) were estimated so that the normalized interpath delay by their mean fits the exponential distribution best. The fitting was performed by evaluating the mean squared error between the empirical curve and the model. An exemplary best-fit linear regression of the mean interpath delay overlaid on the empirical results is illustrated in Fig. 8.

#### D. Channel Model Implementation Recipe

The proposed channel model can be implemented in the following manner. The implementation procedure is the same for the scenarios we covered in this paper. The channel model parameters are summarized in Table III, except for those defined by users, e.g., a Tx–Rx distance.

- 1) *User-dependent inputs*: Specify the Tx–Rx distance  $d$ , radio carrier frequency  $f_c$ , and signal bandwidth  $B$ .
- 2) *Line-of-sight*: Calculate the line-of-sight path delay  $\tau_0 = d/c$  from the Tx–Rx distance and the velocity of light,  $c$ . The line-of-sight path gain is then given by  $\alpha_0 = 1/(4\pi f_c \tau_0)^2$ . The azimuth angle of arrival for the line-of-sight is  $\phi_0 = 0$ .
- 3) *Multipath delays*: Generate multipath delays  $\tau_l$ ,  $l = 1, 2, \dots$ , while  $\tau_l < \tau_c$ . The generation is based on the model (14) where the interpath delays follow the exponential distribution, and therefore, the delay of the  $(l + 1)$ th path yields

$$\tau_{l+1} = \tau_l - \beta_p \ln \xi_u \quad (16)$$

where  $\xi_u \sim \mathcal{U}(0, 1)$ . It should be noted that  $p_l$  in (14), i.e., the probability of observing a hidden path below a noise level, is set to 0 for the convenience of channel generation. At this stage it is assumed that the channel is noise-free, and the noise is added later to a generated channel transfer function. Refer to (15) for the definition of  $\beta_p$ .

- 4) *Multipath powers*: Derive multipath powers  $\alpha_l$  in dB by

$$P_l = P_0 - \frac{10 \log_{10} e}{\beta_0} \tau_l + \sigma_s \xi_n \quad (17)$$



where  $e$  is the Napier's constant and  $\xi_n \sim \mathcal{N}(0, 1)$ . Since the shadow fading is defined stochastically, it is possible to create  $\alpha_l$  greater than the free space path gain, which does not make physical sense. In such cases,  $\alpha_l$  is set to the free space path gain.<sup>2</sup>

- 5) *Multipath angles*: Generate multipath azimuth angles at Rx by  $\phi_l = 2\pi\xi_u$  in radians.
- 6) *Diffuse paths*: If the channel model includes valid parameters for the diffuse spectrum in Table III, set the delay time of diffuse multipaths by  $\tau_{l',d} = \tau_0 + l'/B$ ,  $l' = 1, 2, \dots$ , as long as  $\tau_{l',d} < \tau_c$ . Their powers in dB are given by

$$P_{l',d} = P_d - \frac{10 \log_{10} e}{\beta_d} \tau_{l',d}. \quad (18)$$

It is assumed that the diffuse spectrum is distributed over azimuth angles uniformly, and therefore, diffuse paths with power  $P_{l',d}$  are distributed over all azimuth angles at the Tx side.

- 7) *Channel transfer functions*: Derive the channel transfer functions  $H(f)$  for the frequency range  $f_c - B/2$  and  $f_c + B/2$  by the Fourier transform of the created specular and diffuse paths as

$$\begin{aligned} H(f) = & G_{\text{ant}} G_{\text{pat}}(\phi_0) \sqrt{\alpha_0} e^{-j2\pi f \tau_0} \\ & + G_{\text{ant}} \sum_l G_{\text{pat}}(\phi_l) e^{j2\pi \xi_u} \sqrt{\alpha_l} e^{-j2\pi f \tau_l} \\ & + \sum_{l'} e^{j2\pi \xi_u} \sqrt{\alpha_{l',d}} e^{-j2\pi f \tau_{l',d}} \end{aligned} \quad (19)$$

where  $\alpha_l = 10^{P_l/10}$  denotes the path amplitude in linear scale. Random phase terms are added to the specular and diffuse multipaths,  $G_{\text{ant}}$  is the combined main-lobe gains of the Tx and Rx antennas, and  $G_{\text{pat}}(\phi)$  is a normalized radiation pattern of the Tx antenna with the maximum gain of 0 dB. When the Tx antenna is rotated as was done in our channel sounding, the variation of  $H(f)$  over the orientation of the antenna  $\phi_b$  is defined by replacing  $\phi$  in (19) by  $\phi - \phi_b$ .

Exemplary PADPs from the measurement and the channel model at 70 GHz in the office in-use scenario are illustrated in Fig. 9. The same radiation pattern of the Tx antenna as was used in the measurements was considered in generating the PADP, and therefore, the diffuse paths of the channel model are considered valid. A comparison of the PADPs indicates that the measured PADP has much more clutters than that from the model as the model works as a clutter filter to reduce its complexity. Furthermore, the diffuse paths do not look uniformly distributed over the azimuth angle in measurements, while they do in the model because of the simplicity of the model. This is a shortcoming of the proposed channel model, while their implications on radio link performance will be insignificant since they carry less than 15% of the total power as illustrated in Fig. 5. In Section V-F, delay spread is compared between PDPs from measurements and the channel model to demonstrate the insignificance.

<sup>2</sup>According to our channel model implementation, these cases were observed for less than 1% of the generated specular paths and hence have negligible effects on the statistics of the channels such as delay spread.

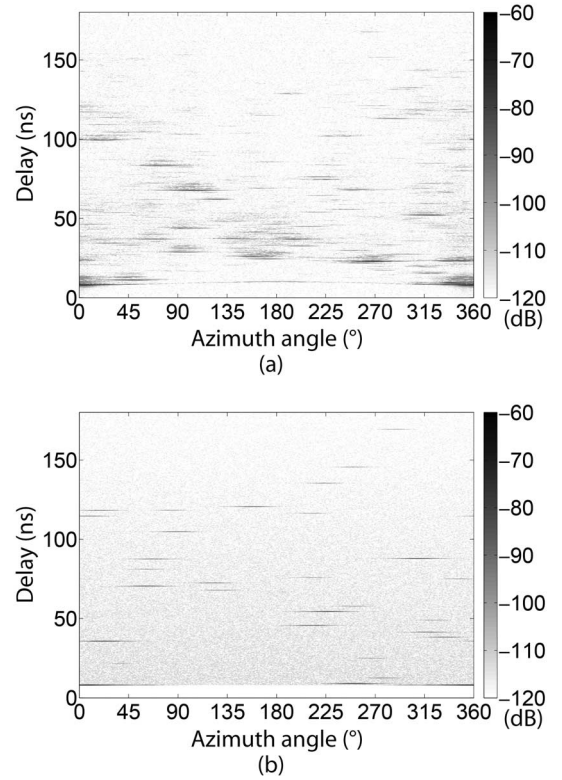


Fig. 9. PADPs from (a) measurement and (b) channel model for the office in-use scenario at 70 GHz.

### E. Discussions on the Channel Model

1) *Difference Between 60 and 70 GHz Channels*: The channel model parameters summarized in Table III provide us with insights on the similarities and differences between 60 and 70 GHz radio channel characteristics. For example, the power decay factor of specular paths,  $\beta_0$  defined in (8), is always smaller at 70 GHz than 60 GHz, indicating that power decay is quicker as the frequency goes higher. On the other hand, the shadow fading values  $\sigma_s$  defined in (9) are almost constant regardless of the frequency and measurement scenarios. Model parameters of diffuse scattering also show notable differences. Though the absolute power level of the diffuse scattering is much weaker at 70 GHz according to  $P_d$  defined in (6), their power decays twice slower than 60 GHz according to  $\beta_d$  values. This is well in contrast to the power decay of specular paths  $\beta_0$ , where 70 GHz channels decays quicker as the delay increases. Finally, looking at  $\beta_s$  defined in (15) for the interpath delay, 70 GHz channels tend to have longer delay lags between two consecutive paths. These insights are partly attributed to the limited dynamic range of the channel sounder. Still, the channel model parameters clearly indicate the difference of 60 and 70 GHz channels mainly in the power decay factor.

2) *Valid Range of the frequency and Tx–Rx Distance*: Note the validity range of the distance and frequency; the channel model parameters were obtained from the measurements with the Tx–Rx range summarized in Table I, and cannot cover the delay beyond  $\tau_c$  because of the limited dynamic range of the channel sounder. RF ranges of the measurements were between 61 and 65 GHz and between 69 and 74 GHz.



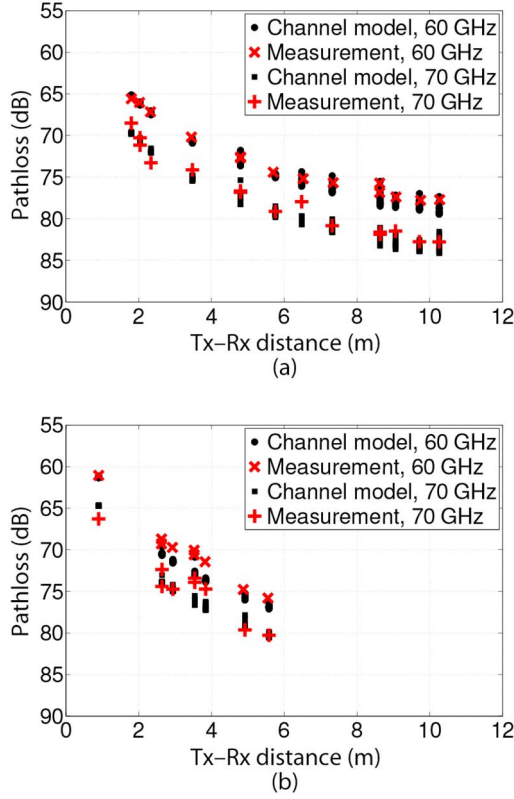


Fig. 10. Comparison of pathloss from measurements and the proposed channel model tested in (a) empty office and (b) station scenarios.

3) *Valid Environments:* The channel model is valid only for the line-of-sight environments since the measurements were mostly performed in such environments. Additional effects leading to obstructed or nonline-of-sight due to human body for example are not a part of this model, but can be easily integrated into this channel model by introducing a path-wise attenuation due to the obstruction. Such attenuation model is available, e.g., in [24].

4) *Antenna Characteristics for the Diffuse Paths:* The diffuse path model implicitly embeds the Tx and Rx antenna characteristics we used in the channel sounding, and therefore, is a valid model only when the user of this channel model assumes the same Tx and Rx antennas as our channel sounding. Otherwise the diffuse path model is faulty and hence should be excluded from the implementation. Even though the diffuse paths are excluded, the amount of the power carried by the diffuse paths is insignificant as discussed in Section IV-C, and therefore, it will not be a critical issue in most cases.

#### F. Validation of the Channel Model

The developed channel model needs to be validated based on the measured channels from which it is derived in order to confirm their consistency. The validation is performed by comparing pathloss and root-mean-square delay spread from measurements and channel models. Since these parameters were not used as a channel model parameter, they are fair metrics for evaluating the consistency between the measurement and model. The pathloss was derived from the PDP by the

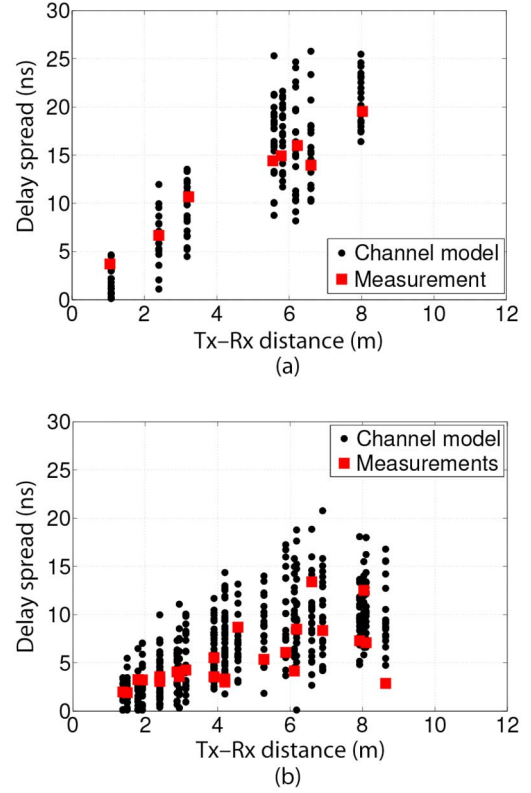


Fig. 11. Comparison of delay spread from measurements and the proposed channel model tested in (a) office in-use scenario at 60 GHz and (b) shopping mall scenario at 70 GHz.

incoherent sum of the power at delay bins, and signal level thresholding of  $\max[(P_{\max}|_{\text{dB}} - 30), T(\tau_n)|_{\text{dB}}]$  was applied in the measurements to consider only dominant signal components;  $P_{\max}$  is the peak power level of the PDP given by the line-of-sight path in our measurements. The same signal level thresholding was used for deriving the metrics from channel model outputs, but under the absence of the noise, i.e.,  $T(\tau_n) = 0$ .

Figs. 10 and 11 illustrate the comparison for two measurement sites at 60 and 70 GHz. For one Tx-Rx distance of the measurements, 20 channels are derived from the model to see their distributions of the metrics. The pathloss in Fig. 10 shows agreement between the measurements and channel model with the standard deviation of 1 and 2 dB approximately for the empty office and station scenarios. The degree of agreement is similar at 60 and 70 GHz in the two sites, while it is better in the empty office than in the station scenario because of dynamics of the environment leading to shadowing of some dominant propagation paths in the measurement. The plots of delay spread in Fig. 11 show much more variation when it is derived from the channel model. The comparison shows that the delay spread of both the measurements and channel model increases as the Tx-Rx distance is longer. Delay spread from the measurements fell within the range of that from the channel model for most cases, demonstrating that the channel model reflects measured channel characteristics. There are cases when the measured value is outside the range of the channel model, e.g., at the largest Tx-Rx separation in shopping mall case at

70 GHz as shown in Fig. 11(b). That is because of the limited dynamic range of the channel sounder, leading to only a handful of meaningful multipaths detected in the measurements. While the channel model is capable of generating multipaths as weak as and even below the noise level, which makes the delay spread is always much smaller than the symbol length of the IEEE 802.11ad standard [25], i.e., 242 ns in the orthogonal frequency division multiplexing including a guard interval and 72.7 ns in the single carrier schemes, suggesting potentially error-free links in propagation scenarios covered in this work.

## VI. CONCLUDING REMARKS

This paper derived a new radio channel model framework and its parameters for various short-range scenarios including offices, a shopping mall, and a station for 60 and 70 GHz radio frequencies. Based on extensive radio channel sounding campaigns, it was found that 1) the dominance of the LOS and specular propagation mechanisms is more apparent in open indoor environments such as a large shopping mall and a railway station than in office environments; and that 2) 70 GHz radio channels suffer from higher losses of both specular and diffuse components than at 60 GHz and show quicker power decay as the propagation delay increases. It was possible to use the same channel model framework for the two frequencies. The proposed framework covers not only specular but also diffuse signals to provide a complete description of the channel. Having parameterized the channel model for the scenarios we covered at the two radio frequencies, their validity was demonstrated by means of pathloss and delay spread. Since the proposed channel model framework is based on the available features of the channel sounding, it does not cover all the multidimensional characteristics of channels such as polarization, elevation, and double-directional characteristics. Extension of the channel model to include those missing features is a subject of our future work.

## ACKNOWLEDGMENT

The authors would like to thank Ms. Y. Miao from Tokyo Institute of Technology, Tokyo, Japan, for assistance in radio propagation measurements.

## REFERENCES

- [1] European Telecommunications Standards Institute. "Fixed radio systems: Characteristics and requirements for point-to-point equipment and antennas," *ETSI EN 302 217 series* [Online]. Available: <http://www.etsi.org/>
- [2] S.-K. Yong *et al.*, "TG3c channel modeling sub-committee final report," IEEE Tech. Rep. 15-07-0584-01-003c, Mar. 2007.
- [3] A. Maltsev *et al.*, "Channel models for 60 GHz WLAN systems," IEEE Tech. Rep. 802.11-09/0334r8, May 2010.
- [4] T. S. Rappaport, J. N. Murdock, and F. Gutierrez, "State of the art in 60-GHz integrated circuits and systems for wireless communications," *Proc. IEEE*, vol. 99, no. 8, pp. 1390–1436, Aug. 2011.
- [5] M. Kyrö, "Radio wave propagation and antennas for millimeter-wave communications," Ph.D. dissertation, Aalto Univ. School of Elect. Eng., Espoo, Finland, Nov. 2012 [Online]. Available: <http://urn.fi/URN:ISBN:978-952-60-4951-9>
- [6] C. Gustafson, K. Haneda, S. Wyne, and F. Tufvesson, "On mm-wave multipath clustering and channel modeling," *IEEE Trans. Antennas Propag.*, vol. 62, no. 3, pp. 1445–1455, Mar. 2014.
- [7] T. S. Rappaport *et al.*, "Millimeter wave mobile communications for 5G cellular: It will work!," *IEEE Access*, vol. 1, pp. 335–349, May 2013.
- [8] T. Rappaport *et al.*, "Broadband millimeter-wave propagation measurements and models using adaptive-beam antennas for outdoor urban cellular communications," *IEEE Trans. Antennas Propag.*, vol. 61, no. 4, pp. 1850–1859, Apr. 2013.
- [9] S. Nie, G. R. MacCartney Jr., S. Sun, and T. S. Rappaport, "72 GHz millimeter wave indoor measurements for wireless and backhaul communications," in *Proc. IEEE Int. Symp. Pers. Indoor Mobile Radio Commun. (PIMRC'13)*, London, U.K., Sep. 2013, pp. 2429–2433.
- [10] M. R. Akdeniz *et al.*, "Millimeter wave channel modeling and cellular capacity evaluation," *IEEE J. Sel. Areas Commun.*, vol. 32, no. 6, pp. 1164–1179, Jun. 2014.
- [11] S. Rangan, T. S. Rappaport, and E. Erkip, "Millimeter-wave cellular wireless networks: Potentials and challenges," *Proc. IEEE*, vol. 102, no. 3, pp. 366–385, Mar. 2014.
- [12] S. Hur *et al.*, "Synchronous channel sounder using horn antenna and indoor measurements on 28 GHz," in *Proc. Int. Black Sea Conf. Commun. Netw. (IEEE BlackSeaCom'14)*, Chisinau, Moldova, May 2014, pp. 83–87.
- [13] K. Haneda, J. Järveläinen, A. Karttunen, M. Kyrö, and J. Putkonen, "Indoor short-range radio propagation measurements at 60 and 70 GHz," in *Proc. 8th Eur. Conf. Antennas Propag. (EuCAP'14)*, Den Haag, The Netherlands, Apr. 2014, pp. 634–638.
- [14] A. Richter, "Estimation of radio channel parameters: Models and algorithms," Ph.D. dissertation, Technische Universität Ilmenau, Germany, 2005 [Online]. Available: <http://www.db-thueringen.de/servlets/DerivateServlet/Derivate-7407/ilm1-2005000111.pdf>
- [15] The 3rd Generation Partnership Project. "Spatial channel model for multiple input multiple output (MIMO) simulations," 3GPP TR 25.996 [Online]. Available: <http://www.3gpp.org/DynaReport/25996.htm>.
- [16] International Telecommunication Union, "Guidelines for evaluation of radio interface technologies for IMT-advanced," Int. Telecommun. Union, Geneva, Switzerland, Tech. Rep. ITU-R M.2135-1, Dec. 2009.
- [17] Flann Microwave. *Standard Gain Horns*, Bodmin, UK [Online]. Available: [http://www.flann.com/Products\\_Home/Antennas/antennas.html](http://www.flann.com/Products_Home/Antennas/antennas.html)
- [18] A. F. Molisch, *Wireless Communications*. Hoboken, NJ, USA: Wiley, 2005.
- [19] M. Kyrö *et al.*, "Statistical channel models for 60 GHz radio propagation in hospital environments," *IEEE Trans. Antennas Propag.*, vol. 60, no. 3, pp. 1569–1577, Mar. 2012.
- [20] H. Yang, P. F. M. Smulders, and M. H. A. J. Herben, "Channel characteristics and transmission performance for various channel configurations at 60 GHz," *EURASIP J. Wireless Commun. Netw.*, vol. 2007, no. 19613, 2007.
- [21] J. B. Andersen, J. O. Nielsen, G. F. Pedersen, G. Bauch, and M. Herdin, "Room electromagnetics," *IEEE Antennas Propag. Mag.*, vol. 49, no. 2, pp. 27–33, Apr. 2007.
- [22] J. Poutanen, J. Salmi, K. Haneda, V.-M. Kolmonen, and P. Vainikainen, "Angular and shadowing characteristics of dense multipath components in indoor radio channels," *IEEE Trans. Antennas Propag.*, vol. 59, no. 1, pp. 245–253, Jan. 2011.
- [23] C. Gustafson, D. Bolin, and F. Tufvesson, "Modeling the cluster delay in mm-wave channels," in *Proc. 8th Eur. Conf. Antennas Propag. (EuCAP'14)*, Den Haag, The Netherlands, Apr. 2014, pp. 804–808.
- [24] M. Jacob *et al.*, "A ray tracing based stochastic human blockage model for the IEEE 802.11ad 60 GHz channel model," in *Proc. 5th Eur. Conf. Antennas Propag. (EuCAP'11)*, Rome, Italy, Apr. 2011, pp. 3084–3088.
- [25] *Part 11: Wireless LAN Medium Access Control (MAC) and Physical Layer (PHY) Specifications—Amendment 3: Enhancements for Very High Throughput in the 60 GHz Band*, IEEE 802.11ad draft, Dec. 2011.



**Katsuyuki Haneda** (S'03–M'07) received the Doctor of Engineering degree from Tokyo Institute of Technology, Tokyo, Japan, in 2007.

Currently, he is an Assistant Professor with Aalto University School of Electrical Engineering, Espoo, Finland. His research interests include high-frequency radios such as millimeter-wave and beyond, wireless for medical and postdisaster scenarios, radio wave propagation prediction, and in-band full-duplex radio technologies.

Dr. Haneda has been serving as an Associate Editor for the IEEE TRANSACTIONS ON ANTENNAS AND PROPAGATION, since 2012, and as an Editor for the Antennas, Channel Models, and Location Area of the IEEE TRANSACTIONS ON WIRELESS COMMUNICATIONS, since 2013. He also served as a Co-Chair of the topical working group on indoor environment and has been an Active Member of European COST Action IC1004 Cooperative radio communications for green smart environments. He was the recipient of the Best Paper Award of the antennas and propagation track in the IEEE 77th Vehicular Technology Conference (VTC2013-Spring), Dresden, Germany, and of the Best Propagation Paper Award in the 7th European Conference on Antennas and Propagation (EuCAP2013), Gothenburg, Sweden.



**Mikko Kyrö** received the M.Sc., L.Sc., and D.Sc. degrees in technology from the Department of Radio Science and Engineering, Aalto University (former Helsinki University of Technology) School of Electrical Engineering, Espoo, Finland, in 2007, 2010, and 2013, respectively.

Since 2013, he has been a Patent Examiner with Finnish Patent and Registration Office, Helsinki, Finland. His research interests include radio channel measurements and modeling as well as antenna designing for millimeter-wave communications

systems.



**Jan Järveläinen** received the M.Sc. degree in technology from Aalto University, Espoo, Finland, in 2011, where he is currently pursuing the D.Sc. degree in radio engineering.

Since 2010, he has been a Research Assistant and Researcher with the Department of Radio Science and Engineering, Aalto University School of Electrical Engineering, Espoo, Finland. His research interests include millimeter-wave radio channel measurements and modeling.



**Jyri Putkonen** received the M.Sc. degree in engineering from Helsinki University of Technology, Espoo, Finland, in 1991.

He is working with the Laboratory of Space Technology as a Research Scientist. Since 1994, he has worked with Nokia as a Program Manager, Head of R&D, and currently doing fifth generation radio system research.



**Aki Karttunen** (M'13) was born in Lahti, Finland, in 1978. He received the Masters of Science (Tech.), the Licentiate of Science (Tech.), and the Doctor of Science (Tech.) degrees in electrical engineering from Aalto University (former Helsinki University of Technology), Espoo, Finland, in 2006, 2009, and 2013, respectively.

He has served at Aalto University since 2002 and is currently a Postdoctoral Researcher with the Department of Radio Science and Engineering. His research interests include millimeter-wave antennas

and millimeter-wave channel measurements, prediction, and modeling.